



Base-free selective oxidation of 5-hydroxymethylfurfural over Pt nanoparticles on surface Nb-enriched Co-Nb oxide

Hao Zhang^a, Runze Zhang^a, Wendi Zhang^a, Bang Gu^a, Qinghu Tang^b, Qiue Cao^a,
Wenhao Fang^{a,*}

^a School of Chemical Science and Technology, National Demonstration Center for Experimental Chemistry and Chemical Engineering Education, Yunnan University, 2 North Cuihu Road, Kunming 650091, China

^b School of Chemistry and Chemical Engineering, Collaborative Innovation Center of Henan Province for Green Manufacturing of Fine Chemicals, Key Laboratory of Green Chemical Media and Reactions, Ministry of Education, Henan Normal University, Xinxiang 453007, China

ARTICLE INFO

Keywords:

Biomass conversion
2,5-Furandicarboxylic acid
Lewis acidic sites
Metal-support interaction
Surface engineering
Synergistic catalysis

ABSTRACT

Constructing functionalized surface for heterogeneous catalysts is vital toward effective conversion of biomass. We show that Pt nanoparticles (ca. 2.1 nm) loaded on Co-Nb bimetallic oxide can efficiently catalyze the aqueous-phase base-free aerobic oxidation of 5-hydroxymethylfurfural to 2,5-furandicarboxylic acid. We ingeniously construct different surface element-distributions over three Co-Nb oxides (Nb@Co, Co&Nb and Co@Nb) with the same bulk composition by changing precipitation sequence of Co and Nb precursors. This strategy allows rationally modulating synergistic interaction and surface acidity of Co-Nb oxides and in return boosts the pristine oxidation activity of loaded-Pt nanoparticles. We use kinetic investigations, comprehensive characterizations, and particularly in situ DRIFT-IR adsorption technique (CO, pyridine and furfural as probe molecules) to unravel the origin of synergistic catalysis. We disclose that Nb⁵⁺-enriched surface can formulate sufficient Lewis acidic sites and stabilize electron-rich Pt⁰ active centers, accelerating the tandem oxidation of HMF and the intermediates. The Co@Nb-Pt catalyst shows the highest productivity of FDCA (25 mmol_{FDCA} mol_{Pt}⁻¹ h⁻¹) among all Pt catalysts in the literature and achieves > 99% yield of FDCA at 110 °C and 10 bar of O₂.

1. Introduction

The direct catalytic conversion of platform compounds is a most effective approach to utilizing biomass sources in fundamental research [1–3]. As a versatile precursor, 5-hydroxymethylfurfural (HMF) can be transformed into many valuable biofuels and chemicals via different roads [4–8], i.e., etherification, esterification, hydrogenation, hydrogenolysis, and partial oxidation. In particular, the selective oxidation of HMF produces 2,5-furandicarboxylic acid (FDCA) [9–14], of which the symmetrical furanic-diacid structure can serve as ideal monomer, instead of the petroleum-based terephthalic acid, to manufacture renewable bio-plastics in the presence of ethylene glycol [15]. Thereby, aerobic oxidation of HMF to FDCA represents a major upgrading process for the furanic platform compounds. As illustrated in the reaction pathway (Scheme S1), production of FDCA from HMF requires continuous oxidations of the OH and C=O groups in HMF and the intermediates [16,17]. This would regrettably result in a complicated distribution of products. In the meantime, the base-free selective

oxidation of HMF to FDCA in O₂ and H₂O has received much attention owing to the greatly desirable green-index [18,19]. No doubt driving such a challenging reaction must necessarily rely on developing highly active and selective heterogeneous catalysts.

Supported-Pt nanoparticles have shown superior catalytic performances toward the aqueous-phase aerobic oxidation of alcohols [27]. Previously, PVP-stabilized quasi-homogeneous Pt nanoparticles were described to efficiently catalyze aerobic oxidation of HMF into FDCA in water without alkali [28]. However, only a few Pt-supported catalysts were investigated in the past decade for the base-free aerobic oxidation of HMF. The catalytic results were summarized in Table 1. Namely, Pt nanoparticles loaded on carbonaceous materials [20–22], metal oxides [23,24] and their composites [25,26] were reported to catalyze the base-free selective oxidation of HMF in water. Generally, 96–100% yield of FDCA can be attained at ca. 100–110 °C under 5–10 bar of O₂. It was disclosed that the nature of support materials can obviously boost the oxidation catalysis of Pt. Specifically, the surface oxygen-containing functional groups at carbonaceous support, oxygen defects and basic

* Corresponding author.

E-mail address: wenhao.fang@ynu.edu.cn (W. Fang).

<https://doi.org/10.1016/j.apcatb.2023.122670>

Received 31 January 2023; Received in revised form 14 March 2023; Accepted 20 March 2023

Available online 21 March 2023

0926-3373/© 2023 Elsevier B.V. All rights reserved.

Table 1

Comparison of the supported-Pt catalysts for the base-free aerobic oxidation of HMF to FDCA in water.

Catalyst	T (°C)	O ₂ (bar)	t (h)	Reuse	Yield (%)	Prod. (mmol _{FDCA} mol _{Pt} ⁻¹ h ⁻¹)	Ref.
Pt/CNT	95	5	14	3	98	7.0	[20]
Pt/C- EDA	110	10	12	5	96	4.0	[21]
Pt/PVP- ACS	110	10	5	10	100	21.8	[22]
Pt/ZrO ₂	100	4	12	n.d.	97.3	5.8	[23]
Pt/NiO	110	10	9	6	100	22.2	[24]
Pt/C-O- Mg	110	10	12	10	97	4.0	[25]
Pt/NC- CeO ₂	110	4	8	6	100	20.0	[26]
Co@Nb- Pt	100	10	6	6	> 99	16.7	this work
Co@Nb- Pt	110	10	4	n.d.	> 99	25.0	this work

sites on oxide support, enabled an enhanced adsorption of reactants. In contrast, the role of acidic sites on Pt-loaded catalysts was barely demonstrated. As a matter of fact, it was roughly mentioned for a Ru/MnCo₂O₄ and a Co₃O₄/Mn_xCoO_y catalysts that both Brønsted and Lewis acidic sites can greatly promote FDCA formation by facilitating activation of the C=O groups [29,30].

It is well known that bimetallic oxides containing multivalent transition metals (i.e., Cu, Mn and Co) could usually show tunable amphoteric and redox properties, leading to strong interaction between different metal ions [13,31–34]. As expected, such material features are highly desirable for the selective oxidation of HMF over a supported-Pt catalyst. In practical operations, varying the metal ratios is quite a common method to tune amphoteric and redox properties of bimetallic oxides. However, controlling the surface element-distributions of bimetallic oxides would be more sophisticated and alternatively determine those vital features. This strategy can in return affect the pristine catalysis power of loaded-Pt nanoparticles. Nevertheless, very few examples can be found in the literature. For instance, the activity of a three-way catalyst (Pt@CeO₂/ZrO₂) was obviously improved by the core-shell configuration of support [35]. It was disclosed that CeO₂ superimposed on ZrO₂ can generate enhanced oxygen-storage capacity and strong metal-support interaction.

In light of this, we develop a Co-Nb bimetallic oxide supported-Pt catalyst for the base-free aerobic oxidation of HMF to FDCA in aqueous phase. We smartly control the surface element-distributions over a group of Co-Nb oxides with the same bulk composition. In addition, the size-controlled synthesis of supported-Pt (ca. 2.1 nm) nanoparticles is realized. These rational constructions enable modulation of the synergistic interaction within components and the Lewis acidity of oxide support, and can differently boost the pristine oxidation activity of loaded-Pt nanoparticles with similar sizes. To the best of our knowledge, such a strategy can be scarcely reported in the literature and the obtained catalytic results are the most outstanding to date. Moreover, we use various advanced techniques and kinetic investigations to deeply understand the unique structure-activity relationship and plausible reaction mechanism, i.e., the synergistic catalysis between Pt and Co₃O₄-Nb₂O₅.

2. Experimental

2.1. Chemicals

All the chemicals were commercialized and used without further treatment. Niobium (V) oxalate hydrate (98%) and sodium hydroxide (97%) from Aladdin®, cobalt (II) nitrate hexahydrate (98%), dihydrogen hexachloroplatinate (IV) hexahydrate (≥ 38% on Pt basis), and

sodium borohydride (98%) from Alfa Aesar, and polyvinyl pyrrolidone (PVP, >98%, M.W. = 10,000) from Tokyo Chemical Industry Co. Ltd. were used for catalyst preparation. 5-Hydroxymethylfurfural (HMF, 99%), 5-hydroxymethyl-2-furancarboxylic acid (HMFA, 98%), 2,5-diformylfuran (DFF, 98%), 5-formyl-2-furancarboxylic acid (FFCA, 98%) and 2,5-furandicarboxylic acid (FDCA, 98%) for catalytic reaction were purchased from Ark Pharm.

2.2. Catalyst preparation

538 mg of niobium (V) oxalate hydrate was dissolved in 100 mL of deionized water, which was marked as Nb precursor. Meanwhile 2.91 g of cobalt (II) nitrate hexahydrate was dissolved in 100 mL of deionized water, which was marked as Co precursor. As illustrated in Scheme S2, three types of Co-Nb bimetallic oxides with the same Nb/Co molar ratio of 0.1 were synthesized as the catalyst supports.

2.2.1. Preparation of Nb@Co support

The pH of Nb precursor was firstly adjusted to 7 using a NaOH solution (1 mol L⁻¹). Then Co precursor was added under stirring at 600 r min⁻¹. After 10 min, the pH of the mixture was further adjusted to 9 using the NaOH solution (1 mol L⁻¹). The resultant suspension was stirred (600 r min⁻¹) at ambient temperature for 2 h. The solids were filtrated and washed by excess deionized water until the pH of the filtrate became neutral. Finally, the solids were calcined at 400 °C for 4 h to obtain the Nb@Co support.

2.2.2. Preparation of Co&Nb support

The Nb and Co precursors were well mixed, and then a NaOH solution (1 mol L⁻¹) was added to adjust the pH of the mixture to 9. The resultant slurry was stirred (600 r min⁻¹) at ambient temperature for 2 h. The solids were collected by filtration and washed using excess deionized water until the pH of the filtrate reached 7. Finally, the solids were calcined at 400 °C for 4 h to obtain the Co&Nb support. In addition, Co₃O₄ and Nb₂O₅ as the referenced supports were prepared by the same procedure.

2.2.3. Preparation of Co@Nb support

Firstly a NaOH solution (1 mol L⁻¹) was used to adjust the pH of Co precursor to 7. Then the Nb precursor was added into the resultant suspension under stirring (600 r min⁻¹). After 10 min, the pH of the mixture was further adjusted to 9 using the NaOH solution (1 mol L⁻¹), afterwards the mixture was stirred at 600 rpm for 2 h. The obtained solids were separated by filtration and washed with excessive deionized water until the pH of the filtrate became 7. The resultant solids were calcined at 400 °C for 4 h to obtain the Co@Nb support.

2.2.4. Preparation of supported-Pt catalysts

The Pt catalysts (theoretical loading: 0.5 wt%) were prepared by a PVP-assisted adsorption method. Typically, with the Co@Nb-Pt catalyst as an example, 0.01 mmol of dihydrogen hexachloroplatinate (IV) hexahydrate and 10 mg of PVP were mixed in 200 mL of deionized water and stirred (600 r min⁻¹) for 0.5 h at room temperature. Subsequently, the Co@Nb support was added and the mixture was stirred for another 1 h. Then, 2.5 mL of freshly prepared NaBH₄ solution (4 mg mL⁻¹) was dropwise added. The suspension was continuously stirred for another 2 h. After that, the solids were recovered by filtration and washed repeatedly by excessive hot (>90 °C) and cold deionized water to remove PVP, Na⁺ and Cl⁻ ions. The solids were finally dried at 80 °C under vacuum overnight to obtain the Co@Nb-Pt catalyst.

2.3. Catalyst characterizations

X-ray diffraction (XRD) was performed on a Rigaku TPR III Diffractometer equipped with a Cu K_α radiation ($\lambda = 1.5418 \text{ \AA}$) and a beam voltage of 40 kV. The XRD patterns in the 2θ domain of 10°–90° were

recorded with a measured rate of 0.02° per 0.2 s. Transmission electron microscopy (TEM) was performed on a Philips-FEITECNAI F30 field-emission electron microscope operated at an acceleration voltage of 300 kV. The samples were previously suspended in ethanol and dispersed ultrasonically. Drops of the suspension were applied on a lacey support film. Energy dispersive spectroscopy (EDS) was conducted on an X-MaxN 80 T IE250 (Oxford). The precise loadings of Pt, Co and Nb were analyzed by inductively coupled plasma mass spectrometry (ICP-MS) using an Agilent 7500a apparatus. The samples were dissolved by sulphuric acid and the resultant solution need be diluted and filtrated before detection. X-ray photoelectron spectroscopy (XPS) was carried out under ultrahigh vacuum on a Thermo Scientific *K-Alpha+* apparatus equipped with an Al K_α radiation. The binding energy (BE) shift due to the surface charging was adjusted based on a reference to the C 1 s line at 284.8 eV. In situ adsorbed pyridine-IR spectroscopy was conducted on a Frontier FT-IR Spectrometer (PerkinElmer) equipped with a MCT detector. The sample in the cell was treated with helium at 300°C for 1 h and then cooled to 30°C . In the meantime, the background spectrum was recorded. Afterwards, the pyridine vapor was switched to the sample for 0.5 h and then a He flow with a rate of 10 mL min^{-1} was introduced to remove the excessive pyridine for 0.5 h. The cell was heated to 150°C with a heating rate of $10^\circ\text{C min}^{-1}$ for 0.5 h and the spectrum of $1400\text{--}1700\text{ cm}^{-1}$ was recorded. In situ time-resolved diffuse reflectance Fourier transform infrared (DRIFT-IR) spectrometry of (i) CO adsorption, (ii) pyridine adsorption, and (iii) furfural adsorption were performed on a Thermo Scientific Nicolet-iS50 FT-IR spectrometer equipped with a MCT detector. (i) For CO adsorption, the sample in the cell was pre-treated at 150°C for 1 h in a He flow (10 mL min^{-1}) and then cooled to 30°C , the background spectrum was collected at this time. Then a pure CO (99.99%) flow was introduced into the cell in a rate of 10 mL min^{-1} for 1 h. Finally, a He flow was switched to remove the free CO molecules, and the spectrum of $1800\text{--}2300\text{ cm}^{-1}$ was recorded at 1, 3, 5, 10, 20, 30, and 60 min (ii) For pyridine adsorption, the Co@Nb oxide in the cell was treated in a He flow (10 mL min^{-1}) at room temperature for 10 min and then the background spectrum was recorded. Then $10\text{ }\mu\text{L}$ of pyridine was sprayed onto the sample. The cell was heated to 100°C (i.e., reaction temperature) within ca. 5 min. Meanwhile the spectrum of $1400\text{--}1550\text{ cm}^{-1}$ was recorded at 1, 5, 10, 20, 30, and 60 min. Notably, the Co@Nb oxide added with $10\text{ }\mu\text{L}$ of furfural was pre-treated at 100°C in a He flow for 1 h to obtain the Co@Nb sample with furfural pre-adsorption. (iii) For furfural adsorption, the sample in the cell was treated at 100°C in a He flow for 1 h and then cooled down to 30°C . The background spectrum was collected. Then $10\text{ }\mu\text{L}$ of furfural was sprayed onto the sample, and the cell was heated to 100°C within ca. 5 min. Meanwhile the spectrum of $1500\text{--}1750\text{ cm}^{-1}$ was recorded at 1, 5, 10, 20, 30, 40, and 60 min.

2.4. Aerobic oxidation of HMF

A batch-type Teflon-lined stainless-steel autoclave (50 mL) was used for the base-free aerobic oxidation of HMF. Typically, 1 mmol of HMF, the catalyst (HMF/Pt = 100, in mole), and 20 mL of deionized water were mixed in the reactor. Afterwards, 10 bar of O_2 was introduced into the reactor after introducing and evacuating O_2 for three times. Then the reactor was placed in an oil bath pre-heated at 100°C with a magnetic stirring at 600 r min^{-1} for 6 h. When the catalytic reaction was over, the reactor was rapidly moved into an ice-bath to cool down. The used catalysts were separated by high-speed centrifugation ($10,000\text{ r min}^{-1}$ for 15 min) and subsequently washed with excessive deionized water and ethanol for three times. Then the obtained solids were dried at 80°C under vacuum overnight before its next use. It should be pointed that a slight and inevitable mass loss of the used catalyst may usually occur during the practical recycling processes, thus a tiny fraction of catalyst was complemented. The time-course experiments in this work were carried out by using the discontinuous clock-reactions, that is, each experiment was recorded at different time.

The reaction mixture was analyzed at 50°C on an Agilent 1260 Infinity HPLC apparatus armed with a Shodex SH-1011 sugar column ($8\text{ mm} \times 300\text{ mm} \times 6\text{ }\mu\text{m}$) and a photodiode array detector (DAD). A diluted H_2SO_4 solution (0.5 mM) was used as mobile phase. The specific wavelengths were set for analyzing the reactant and products, that is, 260 nm for FDCA and HMFCFA, 285 nm for HMF, and 290 nm for FFCA and DFF, respectively. The quantitative analysis was based on an external standard method by calibrating the standard solutions at different concentrations for HMF, HMFCFA, DFF, FFCA and FDCA. The obtained R^2 factors were greater than 0.999. Each reaction was repeated twice to guarantee reproducible results, and the error of data was controlled $\leq 1\%$. Carbon balance was monitored for each reaction, and the values were of 98–100%, indicating that the result was reliable. The conversion of HMF, selectivity of product, initial reaction rate of reactant, and productivity of FDCA were calculated using the following equations (Eqs. (1)–(4)).

$$\text{Conv.}(\%) = \frac{n_{\text{reactant,initial}} - n_{\text{reactant,final}}}{n_{\text{reactant,initial}}} \quad (1)$$

$$\text{Select.}(\%) = \frac{n_{\text{product}}}{n_{\text{reactant,initial}} - n_{\text{reactant,final}}} \quad (2)$$

$$r_{\text{initial}}(\text{mmol mol}_{\text{Pt}}^{-1} \text{s}^{-1}) = \frac{n_{\text{reactant,initial}} - n_{\text{reactant,final}}}{n_{\text{Pt}} \times \text{time}} \quad (3)$$

$$\text{Prod.}(\text{mol}_{\text{FDCA}} \text{mol}_{\text{Pt}}^{-1} \text{h}^{-1}) = \frac{n_{\text{FDCA}}}{n_{\text{Pt}} \times \text{time}} \quad (4)$$

3. Results and discussion

3.1. Co-Nb-Pt catalysts with different surface Nb/Co ratios and similar Pt sizes

As illustrated in Scheme S2, three Co-Nb oxides with different element distributions on the surface are prepared by changing the precipitation sequence of Co and Nb precursors during synthesis. The Nb/Co molar ratio is fixed at 0.1 and the so-obtained oxides are named as Nb@Co, Co&Nb and Co@Nb, respectively. In addition, Co_3O_4 and Nb_2O_5 as the referenced oxides are also laboratory-made. And then, the supported-Pt catalysts are synthesized by a PVP-assisted adsorption method using NaBH_4 as reducing agent.

The structure and morphology of the catalysts were first analyzed. XRD patterns show a well-crystallized cubic Co_3O_4 phase (JCPDS #42-1467) for the Nb@Co-Pt, Co&Nb-Pt and Co@Nb-Pt catalysts, in

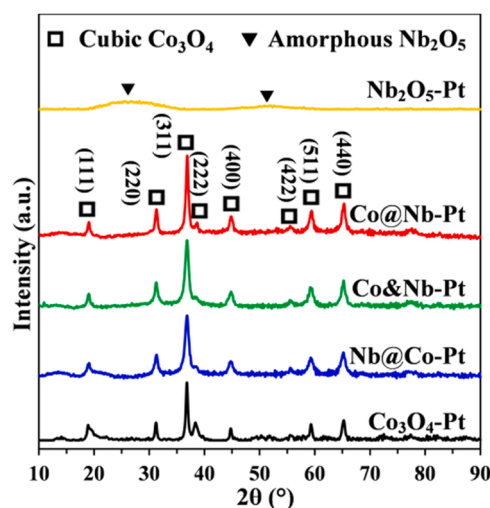


Fig. 1. XRD patterns of the Co_3O_4 -Pt, Nb@Co-Pt, Co&Nb-Pt, Co@Nb-Pt, and Nb_2O_5 -Pt catalysts.

good consistence with the referenced Co_3O_4 -Pt catalyst (Fig. 1). However, no Nb_2O_5 peaks are detected. Even the referenced Nb_2O_5 -Pt catalyst can only display an amorphous and weak Nb_2O_5 phase [36]. Still, Pt diffraction peaks cannot be observed. This may be due to the low loading and/or the high dispersion of Pt nanoparticles. The bright-field TEM images clearly show a composite morphology of nanosphere and nanosheet for the three Pt-catalysts (Fig. S1), probably related to Co_3O_4 and Nb_2O_5 [30,37]. Moreover, the dark-field TEM images obviously reveal uniform and small Pt nanoparticles to be highly dispersed (Fig. 2). The Pt sizes are well confined to 1–4 nm and the mean sizes of Pt are estimated to be ca. 2.1 nm regardless of oxide supports. Moreover, the characteristic lattice fringe of 0.227 nm attributed to the (111) facet of Pt can be clearly identified in the HR-TEM images (Fig. 2) [32]. Therefore, the size-controlled Pt nanoparticles are successfully dispersed on three types of Co-Nb oxides.

Afterwards, the composition and distribution of elements for the Pt-supported catalysts were carefully measured. ICP-MS results disclose that the precise Pt loading (ca. 0.48 wt%) and Nb/Co molar ratio (i.e., 0.1) in each catalyst are almost the same as their theoretical values (Table 2). As is known to all, EDS can be reliable to detect the solid surface beneath ca. 1 μm . As displayed in Fig. 3, EDS elemental maps show homogeneous overlaps of Co and Nb signals but quite different elemental abundances. It is apparent to see a Nb-enriched mapping for the Co@Nb-Pt catalyst but a Co-enriched one for Nb@Co-Pt. Indeed, the quantitative data from EDS confirm the Nb/Co ratio on the Co@Nb-Pt catalyst to be as high as 0.26, whereas that ratio for the Nb@Co-Pt catalyst is of only 0.04 (Table 2). In the meantime, the co-precipitated Co&Nb support exhibits the same element distribution to the bulk Nb/Co ratio. Furthermore, the surface-sensitive XPS technique enables

Table 2

Precise loadings of Pt and Nb/Co molar ratios for the series of Pt-supported catalysts.

Entry	Catalyst	Pt loading (wt %) ICP-MS	Pt loading (wt %) XPS	Nb/Co molar ratio		
				ICP-MS	EDS	XPS
1	Co_3O_4 -Pt	0.48	0.49	n.d.	n.d.	n.d.
2	Nb@Co-Pt	0.47	0.48	0.10	0.04	0.05
3	Co&Nb-Pt	0.49	0.51	0.10	0.11	0.11
4	Co@Nb-Pt	0.47	0.49	0.10	0.26	0.23
5	Nb_2O_5 -Pt	0.48	0.50	n.d.	n.d.	n.d.

precise detection on the outmost surface of a solid. As expected, the results have verified the obviously distinct surface Nb/Co ratios of these three Pt-catalysts. The quantitative data are found to be very close to the EDS data with minor variations. Therefore, 0.5 wt% Pt is effectively loaded on three Co-Nb bimetallic oxides with the same bulk composition. More importantly, an increasing surface Nb/Co ratio (0.05, 0.11, 0.23) is nicely controlled (Fig. 4a).

3.2. Unique behaviors of the series Co-Nb-Pt catalysts

Following that, the base-free oxidation of HMF to FDCA was investigated in water at 100 °C under 10 bar of O_2 , using a series of supported-Pt catalysts (Table 3). It has to be mentioned that all the bare oxide supports are found to be catalytically inactive (Table S1). The referenced Co_3O_4 -Pt catalyst shows a high conversion of HMF (97%) but

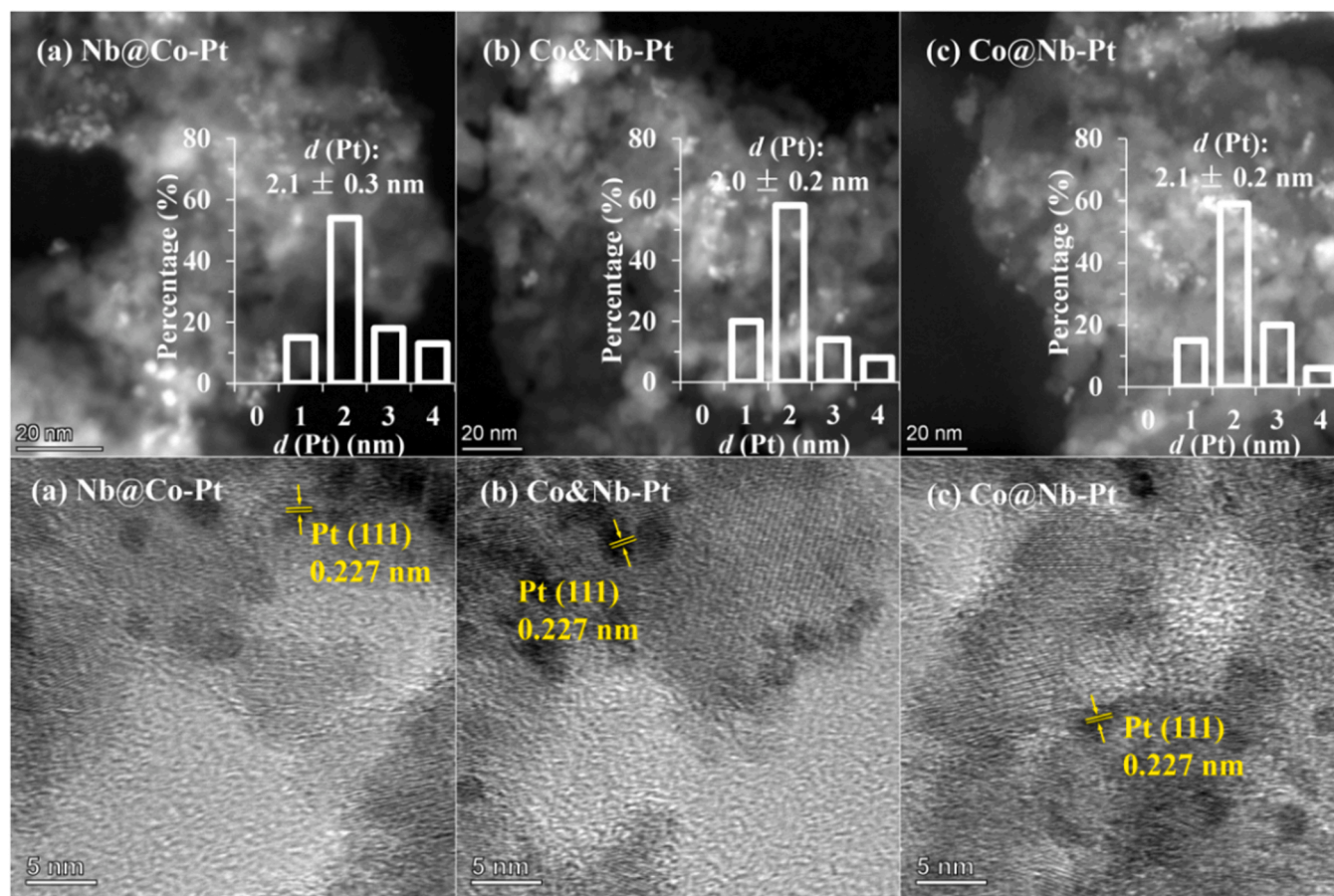


Fig. 2. Dark-field TEM images with insertion of the size distribution of Pt nanoparticles (up) and HR-TEM graphs with marks of the lattice fringe of Pt nanoparticles (bottom) for the Nb@Co-Pt, Co&Nb-Pt, and Co@Nb-Pt catalysts.

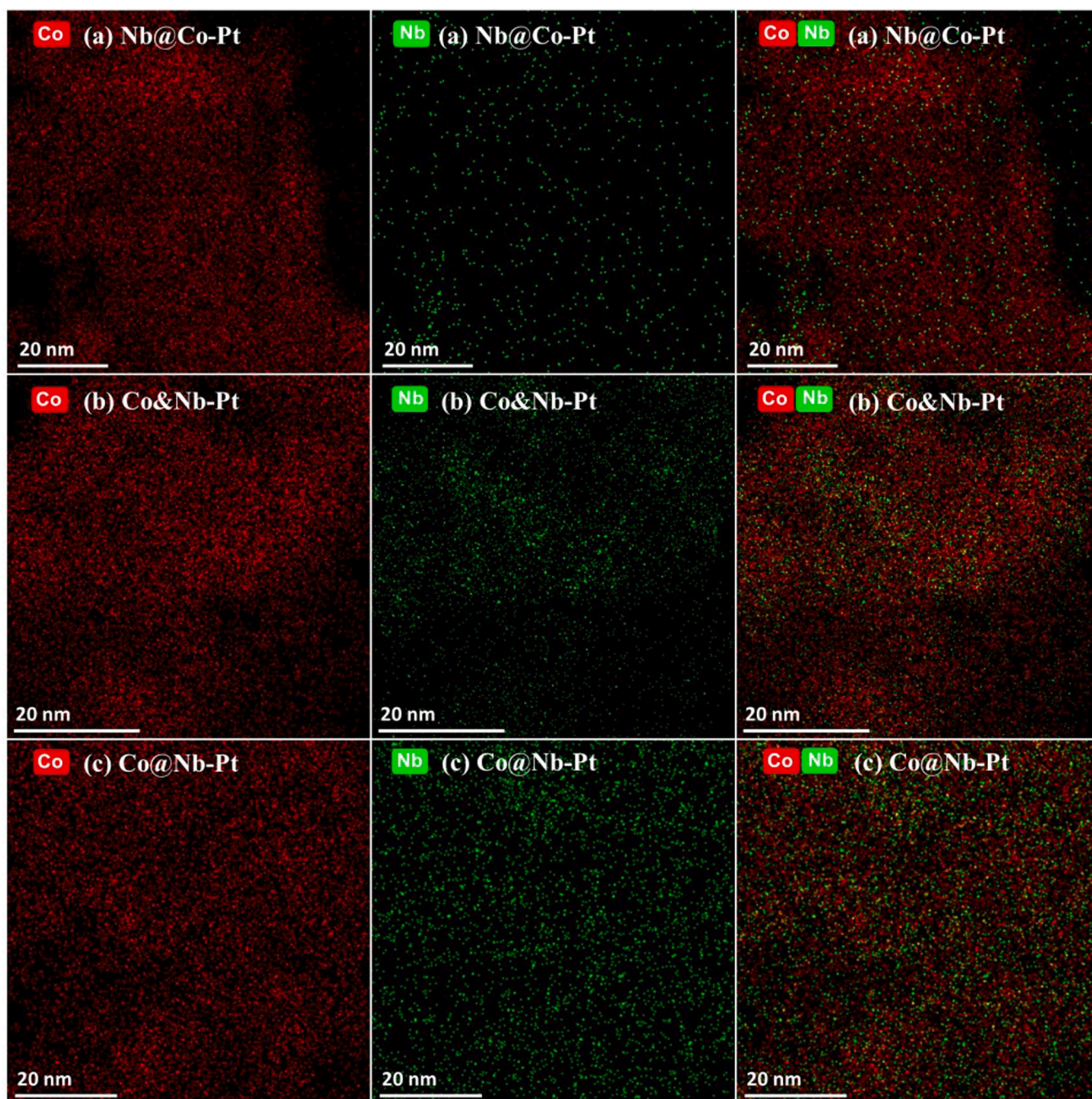


Fig. 3. Color-coded EDS element maps for the Nb@Co-Pt, Co&Nb-Pt, and Co@Nb-Pt catalysts.

a low selectivity of FDCA (40%), while the other referenced Nb₂O₅-Pt catalyst only affords 28% conversion and 2% selectivity of FDCA. Interestingly, the synergy in the Co-Nb bimetallic oxides can obviously improve the performances of supported-Pt catalysts under exactly the same reaction conditions. Despite conversion of HMF can all reach 100%, selectivity of FDCA is greatly influenced by the surface element distribution of the Co-Nb supports (Table 3). Particularly, the surface Nb-enriched Co@Nb-Pt catalyst presents the highest selectivity of FDCA (>99%). In contrast, the Co-enriched surface results in the lowest selectivity of FDCA (55%) on the Nb@Co-Pt catalyst.

Afterwards, the influence of Nb content on the surface was investigated over a series of Co&Nb-Pt catalysts (Nb/Co = 0.05, 0.22 and 0.50) prepared by co-precipitation method. As shown in Table S2, the addition of Nb not only affects conversion of HMF but also selectivity of products.

Conversion of HMF could decline from very high values (97–100%) with increasing the Nb content, i.e., 85% conversion is obtained over the Co&Nb_{0.50}-Pt catalyst. Meanwhile, selectivity of FDCA first increases and then decreases, and the oxidizing intermediates including DFF, HMFA and FFCA are observed. Very interestingly, the co-precipitated Co&Nb_{0.22}-Pt catalyst provides obviously lower selectivity of FDCA compared to the Co@Nb-Pt catalyst (77% versus >99%), even though both catalysts display almost the same surface Nb/Co ratio. It is well known to all that different preparation methods can usually result in different catalytic properties of the final catalysts, for example here the interaction between Co₃O₄, Nb₂O₅ and Pt.

In order to deeply understand the unique synergistic catalysis over the three Co-Nb-Pt catalysts, a series of kinetic experiments were rationally carried out. The time-course reactions show that conversions

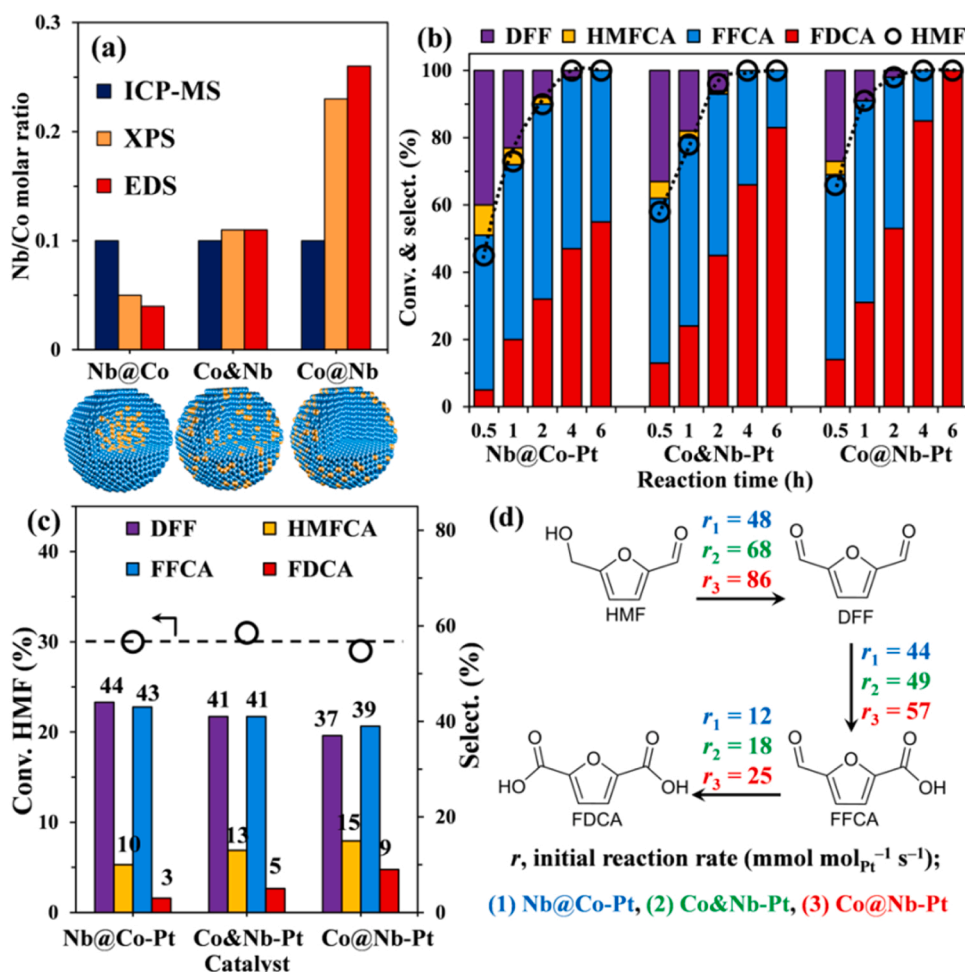


Fig. 4. (a) Bulk and surface Nb/Co molar ratios, (b) time-course reactions and (c) kinetic investigations for the base-free aerobic oxidation of HMF, and (d) initial reaction rates of HMF, DFF and FFCA over the Nb@Co-Pt, Co&Nb-Pt, and Co@Nb-Pt catalysts.

Table 3

Catalytic performances for the base-free aerobic oxidation of HMF in water over a series of supported-Pt catalysts.

Entry	Catalyst	Conv. HMF (%)	Select. (%)			
			DFF	HMFCFA	FFCA	FDCA
1	Co ₃ O ₄ -Pt	97	5	0	55	40
2	Nb@Co-Pt	100	0	0	45	55
3	Co&Nb-Pt	100	0	0	17	83
4	Co@Nb-Pt	100	0	0	0	> 99
5	Nb ₂ O ₅ -Pt	28	52	13	33	2

Reaction conditions: HMF, 1 mmol; HMF/Pt, 100; H₂O, 20 mL; O₂, 10 bar; time, 6 h; temperature, 100 °C.

of HMF on the Nb@Co-Pt, Co&Nb-Pt, and Co@Nb-Pt catalysts continually and rapidly increase to 100% within 4 h. FDCA as the desirable product, as well as DFF, HMFCFA and FFCA as the intermediate is co-observed (Fig. 4b). With the time on stream, FDCA accumulates while DFF and FFCA are converted. These results reveal that both OH and C=O groups in HMF can be simultaneously oxidized on Pt nanoparticles loaded on the Co-Nb oxides and formation of FDCA undergoes a multistep process. Notably, the Co@Nb-Pt catalyst always shows much higher activity and selectivity over the whole reaction, in comparison with the Co&Nb-Pt and Nb@Co-Pt catalysts. It is observed that FFCA being hard to convert over Co&Nb-Pt and Nb@Co-Pt can be totally oxidized into FDCA using the Co@Nb-Pt catalyst within 6 h. Obviously, the Co@Nb oxide allows boosting the selective oxidation catalysis of

supported-Pt for the base-free conversion of HMF to FDCA.

Following that, the intrinsic selectivity of products need be further compared over the three Pt catalysts, when conversion of HMF was controlled at ca. 30%. As shown in Fig. 4c, all the oxidizing products derived from HMF are obtained in the kinetic-controlled region. DFF and FFCA are the dominant products. Thus, HMF → DFF → FFCA → FDCA can be regarded as the major reaction pathway (Scheme S1). Importantly, the Co@Nb-Pt catalyst shows the highest selectivity of FDCA (9%) and HMFCFA (15%) but the lowest one of DFF (37%) and FFCA (39%) among the three Pt catalysts. Therefore, these distinct distributions of products clearly reveal that the Nb-enriched surface for Co-Nb bimetallic oxides can promote FDCA formation on Pt sites by well facilitating oxidation of the C=O groups in HMF, DFF and FFCA.

Afterwards, the initial conversion rates (mmol mol_{Pt}⁻¹ s⁻¹) of HMF, DFF and FFCA were measured over each Pt catalyst (Fig. 4d), respectively. The kinetic data were all collected from the linear conversion rates of the above mentioned substrates during the initial stage (Fig. S2). It is disclosed for each catalyst that $r_{\text{initial}}(\text{HMF}) > r_{\text{initial}}(\text{DFF}) > r_{\text{initial}}(\text{FFCA})$. This trend implies that oxidizing the C=O group in FFCA is the slowest process, thus it can be considered to be the rate-controlling step. Moreover, the Co@Nb-Pt catalyst shows the fastest initial reaction rates for HMF ($r = 86$), DFF ($r = 57$), and FFCA ($r = 25$). These rates are found to be ca. 1.3, 1.1, and 1.4 folds over the Co&Nb-Pt catalyst, and even ca. 1.8, 1.3, and 2.1 folds over the Nb@Co-Pt catalyst. Clearly, the Co@Nb-Pt catalyst enables to greatly accelerate the major reaction pathway and also the rate-limiting step. The Nb-enriched surface in corporation with highly-dispersed Pt nanoparticles plays a vital role in

adsorbing and converting the C=O groups in HMF and the derived intermediates.

In order to get more insights into the role of surface Nb species in the catalytic activity, the apparent activation energy (E_a) for the base-free aerobic oxidation of HMF over the Nb@Co-Pt, Co&Nb-Pt, and Co@Nb-Pt catalysts were further measured. Notably, the kinetic profiles are obtained over these catalysts at different reaction temperatures (90, 100, and 110 °C) in the initial stage and linear relationships are found between kinetic profiles and reaction time (Fig. 5a–c). This kinetic behavior can be the characteristic of the first-order reaction, hence E_a can be calculated by the numerical regression at the assuming of a valid Arrhenius law (Table S3). Obviously, the Co@Nb-Pt catalyst with Nb-enriched surface presents the lowest E_a of 28.6 kJ mol⁻¹, behaving much more active than the Co&Nb-Pt catalyst (E_a = 51.4 kJ mol⁻¹) with evenly-distributed Co-Nb surface and the Nb@Co-Pt catalyst (E_a = 70.2 kJ mol⁻¹) with Co-enriched surface (Fig. 5d). In fact, the apparent activation energy of Pt catalysts for aerobic oxidation of HMF is scarcely investigated in the literature. The low E_a on the Co@Nb-Pt catalyst is much smaller than that of a recently reported Pt/NiO catalyst (E_a = 54.0 kJ mol⁻¹) [24]. This phenomenon is indicative of a fast reaction for HMF oxidation, in agreement with the catalytic behavior of Co@Nb-Pt. These kinetic results demonstrate that the Nb species on catalyst surface allow significantly lowering the energy barrier for the base-free oxidation of HMF on active Pt sites through a more suitable pathway.

Thereafter, the crucial reaction parameters decisive to the catalyst performances were investigated for the Co@Nb-Pt catalyst. As displayed in Fig. S3a, conversion of HMF enables to maintain 100% when the

HMF/Pt ratio grows from 100 to 400. In the meantime, selectivity of FDCA is found to quickly drops from > 99 to 59%, and FFCA as the major by-product (35% in select.) as well as a small amount of DFF are co-generated. This phenomenon shows that an adequate catalyst (i.e., HMF/Pt ratio of 100) is indispensable for effectively converting HMF and FFCA to FDCA. Similarly, the Co@Nb-Pt catalyst behaves sensitive to O₂ pressure (Fig. S3b). By decreasing the pressure from 10 bar down to 1 bar, selectivity of FDCA continuously declines and the oxidizing intermediates are observed. Conversion of HMF can reach 100% even using ambient O₂ pressure (1 bar) over the Co@Nb-Pt catalyst, but product distribution changes dependent on the O₂ introduced. The results show that the OH bond in HMF can be readily oxidized (HMF → DFF) over the Co@Nb-Pt catalyst using ambient O₂ pressure but sufficient O₂ is necessary to drive the further oxidation of HMF-derived intermediates into FDCA.

3.3. Structure-activity correlation and plausible reaction mechanism

In order to unravel the unique structure-activity correlation, some advanced techniques were employed to investigate the catalytic properties of the Co-Nb-Pt catalysts. Firstly, XPS helps precisely analyze the solid surface. As shown in Fig. 6a, the deconvoluted Co 2p_{3/2} core level for the referenced Co₃O₄-Pt catalyst can be assigned to Co³⁺ (ca. 780.0 eV) and Co²⁺ (ca. 781.7 eV) ions and their satellite peaks [38], respectively. The Nb 3d spectrum of the referenced Nb₂O₅-Pt catalyst exhibits two peaks at ca. 207.1 and 209.8 eV attributed to the typical Nb⁵⁺ ions in Nb₂O₅ (Fig. 6b) [36]. With the growth of surface Nb/Co

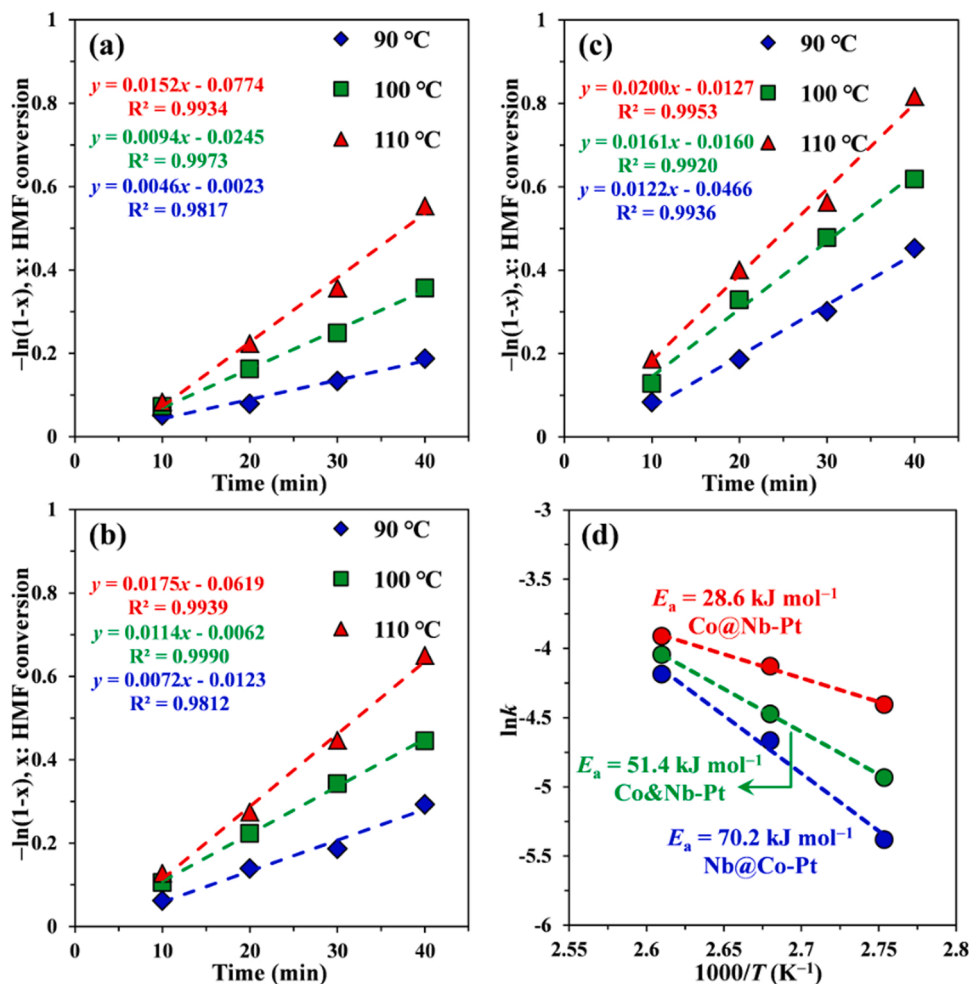


Fig. 5. (a–c) Kinetic profiles and (d) Arrhenius plots for the base-free aerobic oxidation of HMF over the (a) Nb@Co-Pt, (b) Co&Nb-Pt, and (c) Co@Nb-Pt catalysts. Reaction conditions: HMF/Pt, 400; H₂O, 20 mL; O₂, 10 bar.

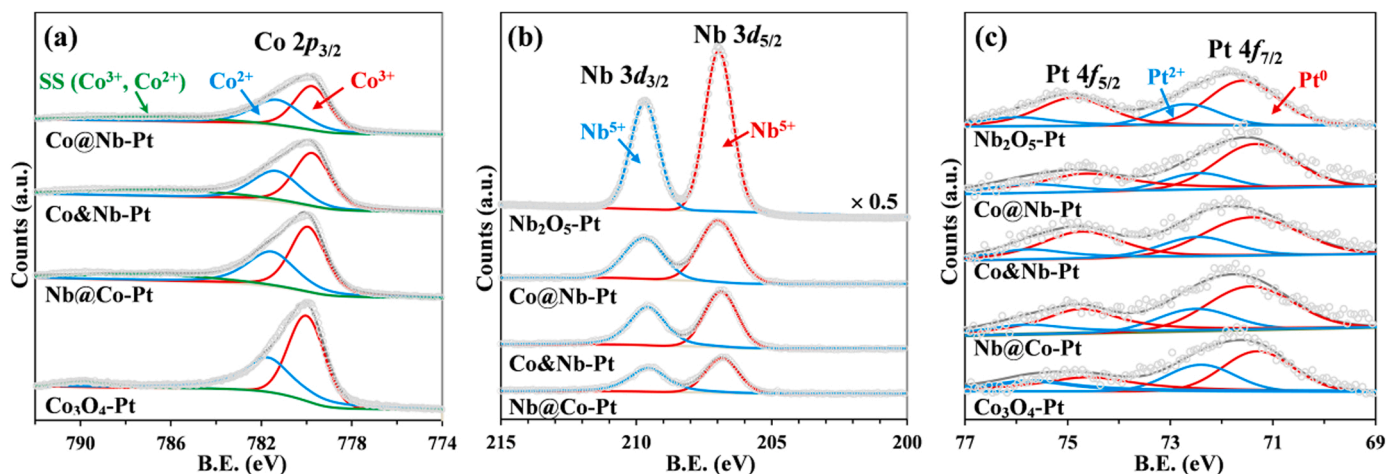


Fig. 6. Deconvoluted XPS spectra of (a) Co $2p_{3/2}$, (b) Nb $3d$, and (c) Pt $4f$ core levels for the Co_3O_4 -Pt, Nb@Co-Pt, Co&Nb-Pt, Co@Nb-Pt, and Nb_2O_5 -Pt catalysts.

ratio, the binding energy of Nb ions gradually increases and reaches the same value of Nb_2O_5 -Pt, while that of Co ions gradually decreases compared to those of Co_3O_4 -Pt (Table S4). This phenomenon indicates an electron transfer from Nb to Co on the bimetallic Co-Nb oxides, leading to electron-deficient Nb^{5+} species on surface of the Co@Nb-Pt catalyst. Meanwhile, typical lattice oxygen species (O_{latt} : O^{2-}) at ca. 530.1 eV and adsorbed defective oxygen species (O_{ads} : O^- and O_2^-) at ca. 531.6 eV are recorded on the surface of all Pt catalysts (Fig. S4). The Pt $4f_{7/2}$ core levels for the referenced Co_3O_4 -Pt and Nb_2O_5 -Pt catalysts are resolved into two peaks that can be ascribed to Pt^0 (71.5 and 71.6 eV) and Pt^{2+} (72.6 and 72.7 eV) species [32], respectively (Fig. 6c). Interestingly, the binding energies of Pt on the series Co-Nb-Pt catalysts slightly decrease by increasing the surface Nb/Co ratio (Table S4). This observation can be caused by the electron transfer and strong interaction between Pt and support. Moreover, the fraction of Pt^0 obviously rises with the growth of surface Nb/Co ratio, and the highest fraction of Pt^0 (77%) is attained on the Co@Nb-Pt catalyst (Table S5). Hence, Nb^{5+} -enriched surface induces formation of sufficient electron-rich Pt^0 sites.

In order to clearly explore the electron transfer process between Nb, Co and Pt, some more XPS analyses were carried out on the bare carriers (i.e., Nb@Co, Co&Nb, and Co@Nb). As shown in Fig. S5 and Table S6, when the surface ratio of Nb/Co grows, the binding energy of Nb ions slightly increases while those of Co ions gradually decrease. This observation is consistent with the property of Pt-supported catalysts (Table S4). The variation of binding energies confirms the existence of electron transfer from Nb to Co in the bare Nb-Co bimetallic oxides, generating electron-deficient Nb^{5+} species. The formation mechanism can be originated from the interaction between Nb_2O_5 and Co_3O_4 during preparing the bimetallic oxides. And the stronger interaction would make this effect more pronounced, i.e., the behavior of the Co@Nb carrier. Notably, the synergistic interaction between Nb_2O_5 and Co_3O_4 can in return boost the electron transfer from support material to Pt. Thus electron-rich Pt^0 species are generated on the optimum Co@Nb-Pt catalyst.

Thereafter, the nature and number of acidic sites on the Co-Nb supports were accurately analyzed by in situ adsorbed pyridine-IR spectroscopy. As displayed in Fig. 7, two strong bands at ca. 1445 and 1597 cm^{-1} are clearly observed. These signals can be attributed to pyridine adsorption on the Lewis acidic sites related to surface Nb and/or Co ions in low-coordination state [39]. Notably, Co_3O_4 displays different band position and weak intensity for Lewis acidic sites (Table 4), which implies that the surface Lewis acidity of Co-Nb bimetallic oxides can be mainly associated with Nb ions. The slight increase of Nb/Co ratio on surface results in an obvious growing of Lewis acidity. While a weak band at ca. 1544 cm^{-1} can be assigned to adsorbed pyridine on the

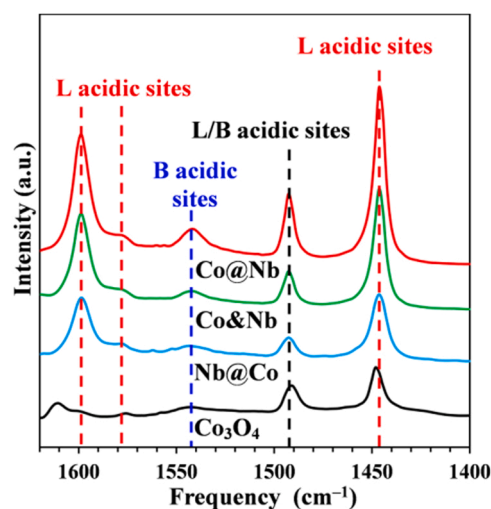


Fig. 7. Adsorbed pyridine-IR spectra of the Co_3O_4 , Nb@Co, Co&Nb, and Co@Nb oxides.

Table 4

Acidity of the Co_3O_4 and Co-Nb oxide supports measured by in situ adsorbed pyridine-IR spectroscopy.

Entry	Catalyst	Acidity (mmol g^{-1})			Fraction of Lewis acidity
		Lewis	Brønsted	Total	
1	Co_3O_4	0.12	0.05	0.17	0.71
2	Nb@Co	0.17	0.04	0.21	0.81
3	Co&Nb	0.31	0.06	0.37	0.84
4	Co@Nb	0.49	0.08	0.57	0.86

Brønsted acidic sites due to surface OH groups [39]. Besides, a moderate band at ca. 1487 cm^{-1} can be originated from the co-adsorption of pyridine on Lewis and Brønsted acidic sites [39]. Although Lewis and Brønsted acidity simultaneously increases with the growth of surface Nb/Co ratio, the former one is certainly found to be dominant, i.e., the proportion can reach 0.81–0.86 (Table 4). Thereby, the Co@Nb oxide with Nb^{5+} -enriched surface shows the highest Lewis acidity (0.49 mmol g^{-1}) among the Co-Nb bimetallic oxides.

Furthermore, in situ DRIFT-IR using CO as probe molecule was used to investigate the outermost Pt sites on catalysts. CO is intensively used as simplified model for the C=O bond in an organic reactant. As shown in Fig. 8a–c, the time-resolved DRIFT-IR spectra disclose for all the Co-

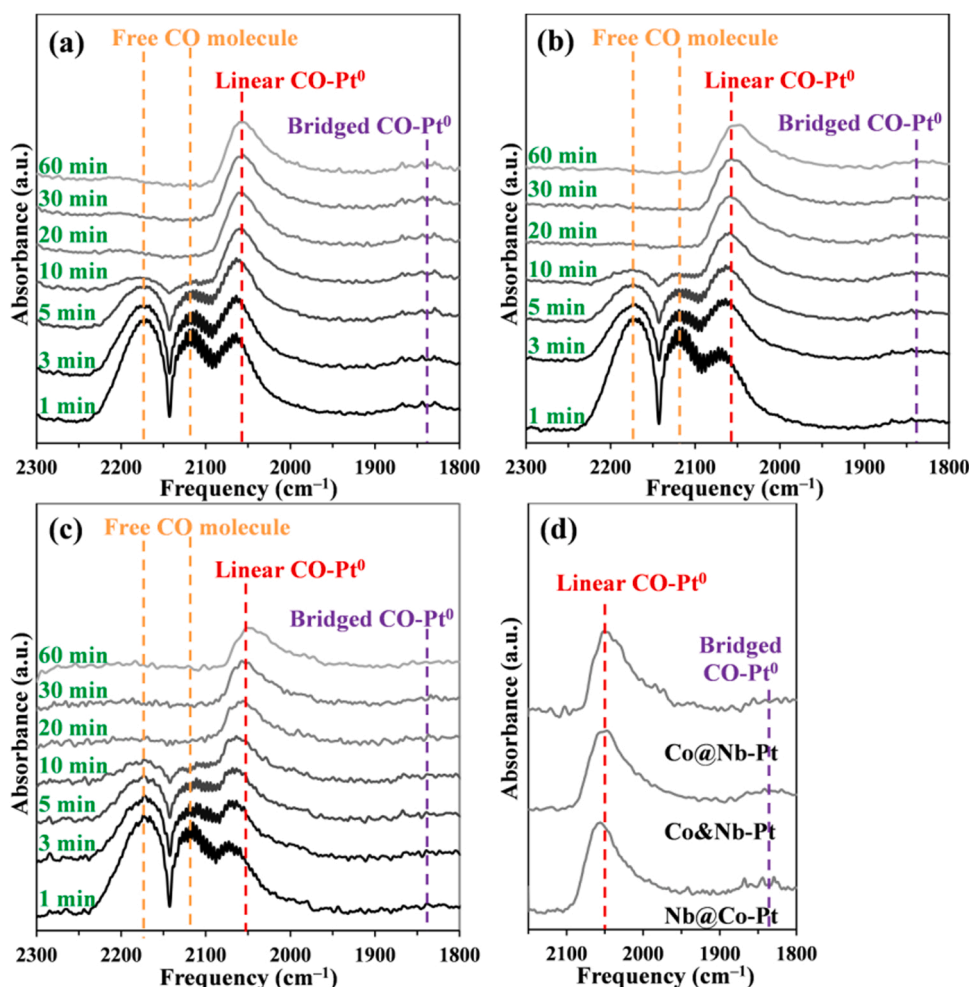


Fig. 8. Time-resolved DRIFT-IR spectra of CO adsorption for the (a) Nb@Co-Pt, (b) Co&Nb-Pt, and (c) Co@Nb-Pt catalysts, and (d) the adsorption spectra after He purge for 60 min.

Nb-Pt catalysts that two intense bands at ca. 2115 and 2170 cm^{-1} due to the typical free or physisorbed CO molecules can be eliminated after 20 min with the purge of a He flow [24]. In the meantime, an intense band at ca. 2075 cm^{-1} and several small bands at 1800–1900 cm^{-1} can well retain after 60 min of He purge. These signals can be attributed to linear and bridged adsorption of CO molecules on Pt^0 sites [24], respectively. Moreover, the main adsorption band clearly shifts to a lower frequency (15–20 cm^{-1}) over time from 1 to 60 min. This phenomenon probably indicates the activation of CO molecules on Pt^0 [24]. Further inspection on the stabilized spectra of CO adsorption after 60 min could provide information on the detailed differences of metallic Pt sites on three Co-Nb oxides for CO adsorption. Importantly, the Co@Nb-Pt catalyst shows a major redshift versus Nb@Co-Pt for the main band of Pt^0 (Fig. 8d), which can be originated from the high electron density on the Pt^0 sites, in well consistent with XPS results. In fact, it has been demonstrated that metallic Pt sites with higher electron density can benefit aerobic oxidation of carbonyl compounds [40]. Therefore, the Nb@Co-Pt catalyst as expected exhibits the optimum oxidation performance.

The structure-activity correlation was then discussed with respect to Pt species and Lewis acidity. As plotted in Fig. 9, the initial reaction rates (r_{initial}) for aerobic oxidation of HMF, DFF and FFCA are proportional to the fraction of surface Pt^0 sites. And moreover, the electron-sufficient Pt^0 sites on the Co@Nb-Pt catalyst are evidenced to effectively adsorb and activate the C=O groups in HMF, DFF and FFCA. This can be well interpreted by the strong interaction between electron-rich Pt^0 species and the C=O group through back bonding of $\pi^*\text{C}=\text{O}$ with Pt species

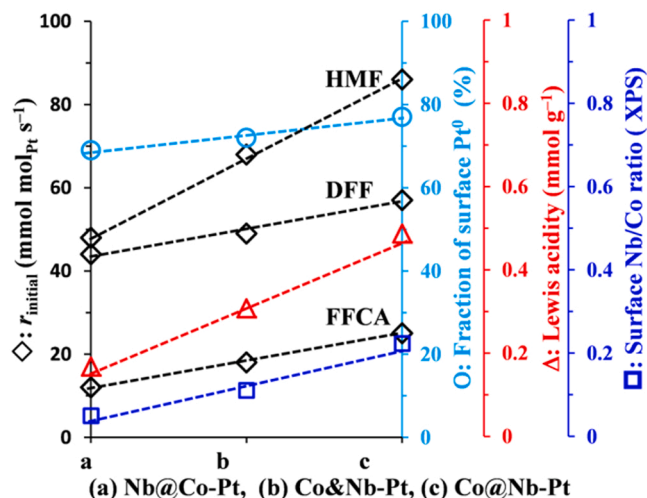


Fig. 9. Relationship between the r_{initial} for the base-free aerobic oxidation of HMF, DFF and FFCA and the fraction of surface Nb/Co ratio, Lewis acidity and Pt^0 in the series supported-Pt catalysts.

[40]. In the meantime, Brønsted and especially Lewis acidic sites are vital to promote FDCA formation from HMF. To be recalled, the $\text{Co}_3\text{O}_4\text{-Pt}$ catalyst only affords 40% selectivity of FDCA at 97%

conversion of HMF, DFF and FFCA as by-product are co-generated (Table 3). The result implies that the Lewis acidity due to Co ions is inadequate to convert C=O groups in HMF, DFF and FFCA to a COOH group in corporation with active Pt⁰ sites. Moreover, Lewis acidity directly linked to the surface Nb⁵⁺ species is observed to proportionally decide the initial conversion rates of HMF, DFF and FFCA (Fig. 9). The electron-deficient Nb⁵⁺ species on the Co@Nb-Pt catalyst may provide enhanced electron acceptability thus can afford stronger Lewis acidity [41]. In the literature, it was proposed for the selective oxidation of HMF to DFF over a Mn₆FeO₄ catalyst that the OH group can first adsorb onto surface Mn⁴⁺ ions (Lewis acid) through sharing a lone pair [42]. In another case for the selective oxidation of HMF to FDCA using a CoO_x@Nb-zeolite catalyst, Nb⁵⁺ ions (Lewis acid) helped dehydrogenation of the geminal diol intermediate generated from C=O group to yield COOH group [43].

In light of this, in situ pyridine-IR spectroscopy was carried out to get insights into the unique role of surface Lewis acidic sites of the Co@Nb support on adsorption and activation of the C=O bonds in HMF and its derived intermediates. In this case, furfural as the most suitable probe-molecule is selected. That is because the molecular structure and reactive bonds of furfural (i.e., C=O and C=C) are quite similar to HMF and its oxidizing intermediates, but the interference of C–OH and/or COOH substituents attached to furan ring can be reasonably avoided. As shown in Fig. 10a, the typical Co@Nb support alone (i.e., without furfural pre-adsorption) can adsorb pyridine in a very short time. Two characteristic bands can be respectively assigned to pyridine adsorbed on Lewis acid sites (ca. 1443 cm⁻¹) and co-adsorbed on Lewis and Brønsted acid sites (ca. 1487 cm⁻¹) [39]. Notably, the intensity of these bands continuously decreases during 20 min with He purge (Fig. 10a,c), which can be due to the removal of free and/or physically adsorbed pyridine from the solids. After 20 min, the pyridine adsorption becomes stabilized in He flow. This finding demonstrates that the presence of abundant Lewis acidic sites due to Nb⁵⁺ ions on the Co@Nb surface allows effectively anchoring the chemisorbed pyridine molecules. When furfural is pre-adsorbed on the Co@Nb support, pyridine can be co-adsorbed on the solids. But the intensity of pyridine adsorption is found to sharply declines and nearly all pyridine molecules can be desorbed from the surface of Co@Nb support (Fig. 10b,c). This observation evidences that the pre-adsorbed furfural molecules have occupied the Lewis acidic sites on the Co@Nb support, thus the subsequently introduced pyridine is hardly adsorbed by the oxide surface [44]. Therefore, it can be presumed that

the surface Nb⁵⁺ ions as Lewis acid sites are probably responsible for adsorption of HMF, DFF, and FFCA.

In order to unravel the adsorption behavior of HMF and its oxidizing intermediates on the series of Pt-supported catalysts, in situ DRIFT-IR of furfural adsorption was firstly performed on the bare Nb@Co, Co&Nb and Co@Nb supports (Fig. 11a–c), as well as the referenced Co₃O₄ and Nb₂O₅ supports (Fig. S6). The time-resolved spectra obtained on all the oxides present three typical bands at ca. 1570, 1674, and 1697 cm⁻¹, which can be assigned to the C=C bonds in furan ring, the C=O bond attached to furan ring chemically or physically adsorbed on the oxide surface [44,45], respectively. Notably, these bands are found to gradually decrease with He purge and then become stabilized. It has been shown by theoretical studies that the flat-adsorption mode can be optimized for furfural [46] and HMF [47] molecules, where the C=C bond gets parallelly close to and interacts with the oxide surface. Thereby, the C=O bond in furfural can be simultaneously adsorbed through the interaction of O atom with the oxide surface (i.e. the band at 1674 cm⁻¹) [48]. These important observations imply the co-adsorption of C=C and C=O bonds in HMF and the derived intermediates on the Co-Nb oxide supports.

Further comparison of the spectra obtained at 60 min shows different adsorption capacities of furfural on all the supports (Fig. 11d). The intensity of C=C bond adsorption obviously declines with decreasing the surface Nb loading. As expected, Nb₂O₅ presents the highest adsorption of furfural whereas Co₃O₄ displays the lowest value. This phenomenon reveals that surface Nb⁵⁺ species as Lewis acidic sites can promote adsorption of furfural on an oxide via the enhanced interaction with the C=C bonds in furan ring. The Co@Nb support with Nb⁵⁺-enriched surface presents the maximum Lewis acidic sites among three Co-Nb oxides, without no doubts, it can be readily to adsorb and stabilize HMF and its oxidizing intermediates.

Following that, furfural adsorption was conducted on the optimum Co@Nb-Pt catalyst to understand the role of Pt⁰ sites on oxidation of the C=O bond. Time-resolved spectra show stabilized adsorption of furfural after 20 min, as reflected by two adsorption bands due to the C=C bonds in furan ring and the chemisorbed C=O bond (Fig. 11e). More importantly, the Co@Nb-Pt catalyst presents a significant redshift (ca. 30 cm⁻¹) for the chemisorbed C=O bond in comparison with the Co@Nb support, but the peak position for adsorbed C=C bonds remains unchanged on both solids (Fig. 11f). This unique observation reveals that Pt⁰ sites are vital for the Co@Nb-Pt catalyst to adsorbing and

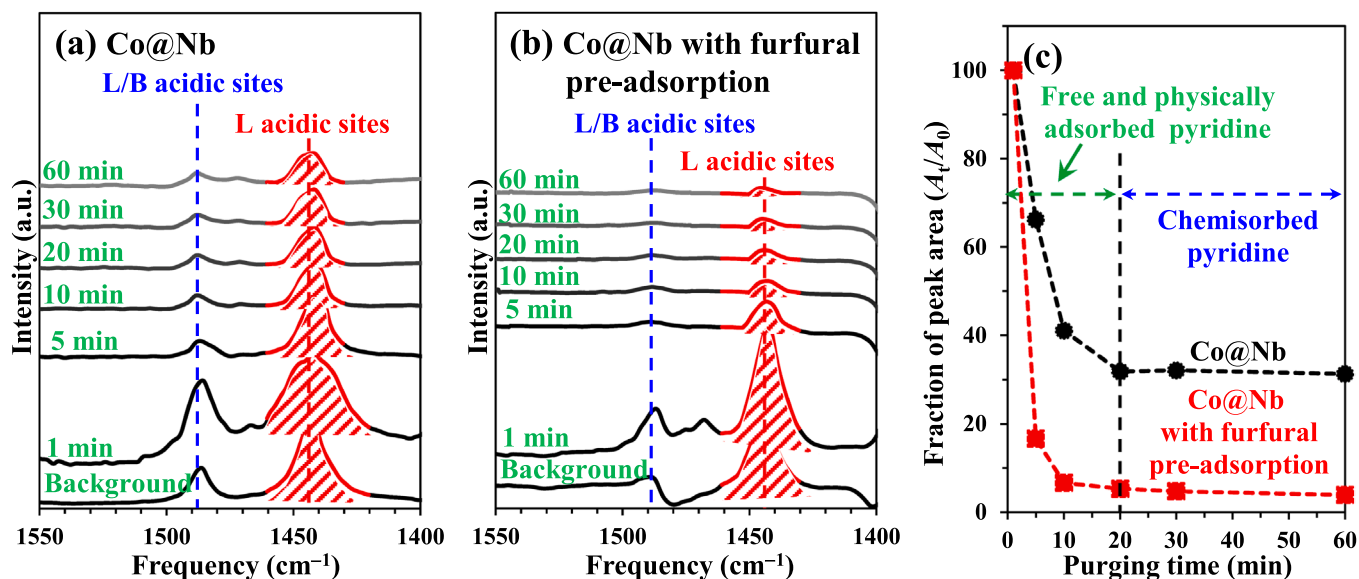


Fig. 10. (a) Time-resolved pyridine-IR spectra of the Co@Nb oxide without furfural adsorption and (b) with furfural pre-adsorption. (c) Relationship between the normalized peak areas over the peak area obtained at 1 min of the band at ca. 1445 cm⁻¹ and the purging time.

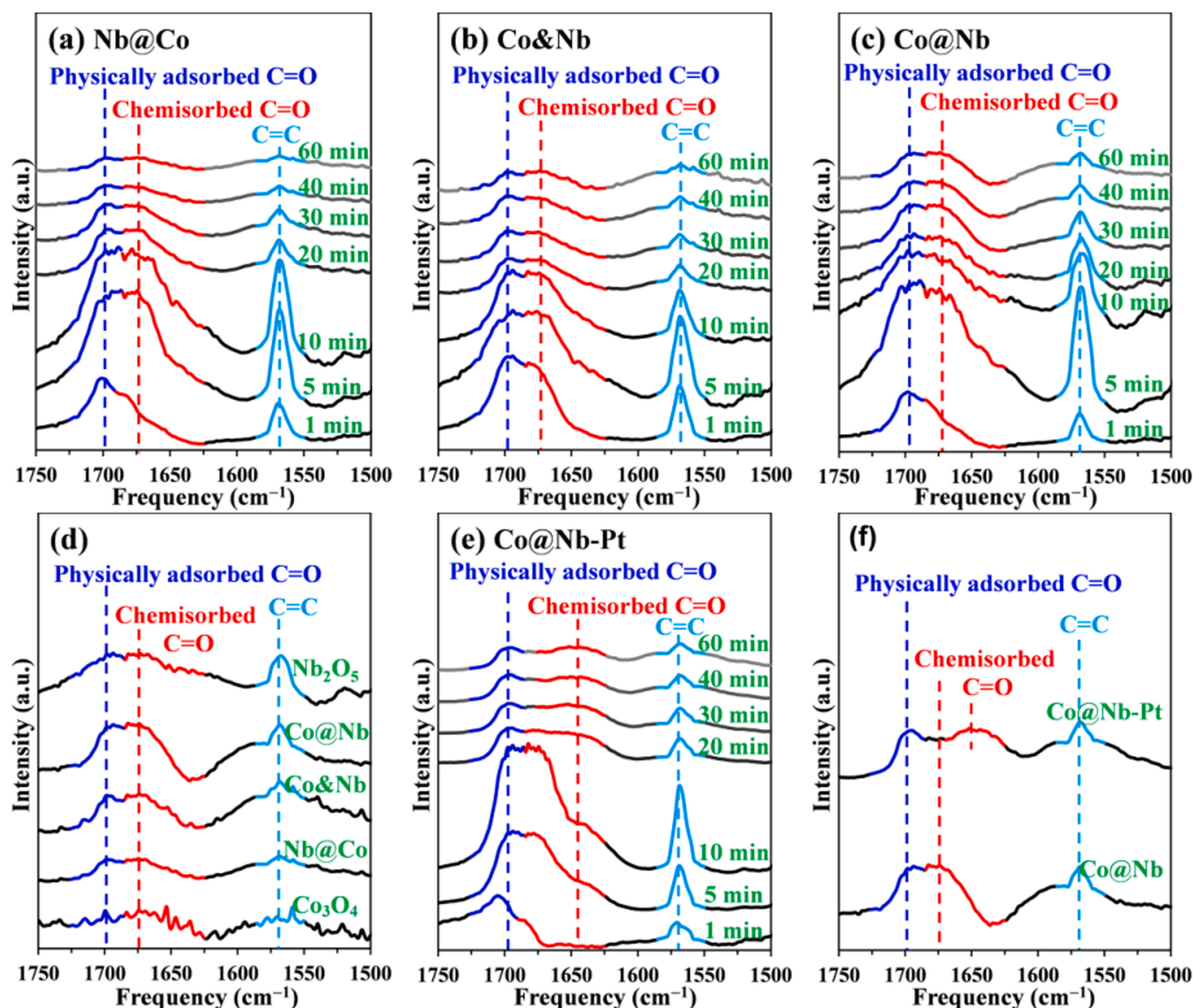
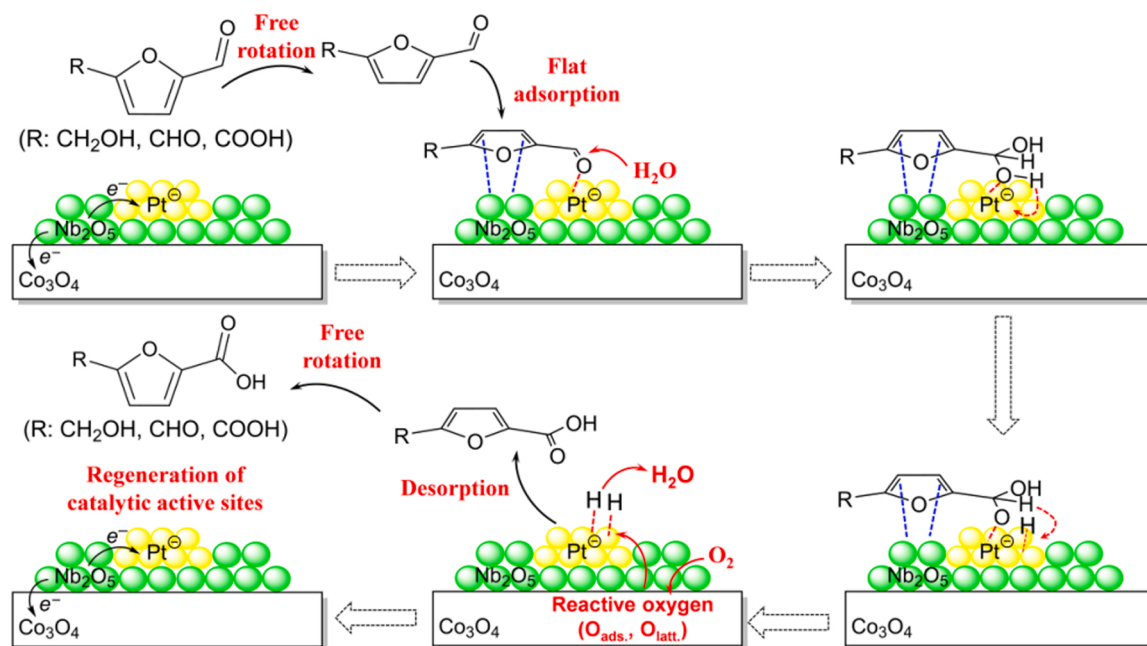


Fig. 11. Time-resolved DRIFT-IR spectra of furfural adsorption at 100 °C on the (a) Nb@Co, (b) Co&Nb and (c) Co@Nb supports, and (d) the spectra of all the oxide supports with He purge after 60 min (e) Time-resolved DRIFT-IR spectra of furfural adsorption at 100 °C on the Co@Nb-Pt catalyst, and (f) the comparative spectra of Co@Nb and Co@Nb-Pt after 60 min of He purge.

activating the C=O bond in furfural. In short, all the direct spectroscopic evidences demonstrate that surface Lewis acidic sites (i.e., Nb^{5+} species) can facilitate the approach of HMF and its oxidizing intermediates to the surface of Co@Nb-Pt catalyst through an optimized adsorption configuration (i.e., flat-adsorption of C=C bonds in furan ring), and this enables to simultaneously stabilize the electron-rich Pt^0 species as catalytic active sites to adsorb and activate the C=O bonds in HMF, DFF and FFCA with the presence of O_2 via a lower energy barrier.

In light of all the above analyses, the plausible reaction mechanism was openly discussed. Notably, the illustration focuses on the major reaction pathway (i.e., $\text{HMF} \rightarrow \text{DFF} \rightarrow \text{FFCA} \rightarrow \text{FDCA}$) and highlights the transformation of C=O bonds in HMF, DFF and FFCA during tandem oxidation catalysis. It is widely believed that Pt^0 species are the catalytic active sites for the base-free aerobic oxidation of HMF [20–26]. In this work, Pt loaded on the Co@Nb oxide is confirmed to be essential to converting HMF. The first step has been well demonstrated for Pt-catalyzed oxidation of alcohols [49]. Specifically, metallic Pt sites enable to adsorb and cleave the O–H bond in HMF molecule to form Pt-alkoxide intermediate and adsorbed hydrogen in form of Pt–H hydride [50]. In the same time, O_{latt} species on the Co@Nb support could

also assist adsorption of H atom in the C–OH bond. After then, the Pt-alkoxide intermediate is converted to a C=O bond via β -H elimination. Hence DFF is formed. As described in Scheme 1, the aqueous-phase aerobic oxidation of C=O bonds in HMF and its oxidizing intermediates to a COOH bond is also catalyzed by Pt^0 species. Firstly, a planar HMF or HMF-derived molecule would parallelly get close to the catalyst surface through a free rotation. Afterwards, Pt^0 active sites can react with O atom in the C=O bond of HMF, DFF and FFCA so as to adsorb this reactive bond. Notably, it has been shown that electron-sufficient Pt^0 sites are beneficial to aerobic oxidation of carbonyl compounds [40]. More importantly, the abundant surface neighboring Nb^{5+} ions as Lewis acidic sites allow strongly promoting adsorption of the substrate by interacting with the conjugate C=C bonds in furan ring. Meanwhile, the transformation of C=O bond in HMF and its derived intermediates to COOH bond occurs by forming a gem-diol and a hemiacetal intermediate with the participation of H_2O molecules and reactive oxygen species (i.e., O_{ads} and O_{latt}). An earlier work on Pt-catalyzed aerobic oxidation of HMF disclosed the participation of H_2O in formation of a gem-diol intermediate by ingeniously using isotopically marked H_2^{18}O molecules [28]. Recently, the direct spectroscopic evidence for H_2O involvement in



Scheme 1. Mechanistic illustration for the aqueous-phase aerobic oxidation of C=O bond in HMF and its oxidizing intermediates over the Co@Nb-Pt catalyst.

aerobic oxidation of HMF to FDCA was observed using in situ DRIFT-IR technique on a Au/Ni_xCo_{1-y}O_y catalyst [13]. These findings demonstrated that H₂O can be dissociated to OH⁻ ions and the successive nucleophilic addition of OH⁻ ions to C=O bond could form a gem-diol intermediate. After then, the gem-diol can be further converted to a hemiacetal intermediate and finally a COOH bond via continuous dehydrogenation. In this process, the reactive O_{ads} and O_{latt} species on the surface of Co@Nb oxide are essential and enable to react with the adsorbed H atom on Pt⁰ sites to produce H₂O, which realizes the regeneration of catalytic active sites and the closing of catalytic cycle, accompanied with desorption of a product. It has been clearly verified in the literature that the reactive oxygen species can be generated and supplemented by molecular O₂ through activation and dissociation at oxygen vacancies of an oxide support [13,17,24].

3.4. Reusability and comparison study

Finally, the catalytic stability and reusability was inspected. The present Co@Nb-Pt catalyst shows excellent reusability during six cycles not only under the optimized reaction conditions but also within the kinetic-controlled stage (Fig. S7a). This operation can avoid observing a false stability by using the saturated catalytic results. Because any deactivation of a catalyst can be usually reflected at the initial stage. In addition, the leaching test based on hot-filtration experiment indicates no loss of Pt as well as Nb and Co from the catalyst to the reaction mixture (Fig. S7b). The reaction cannot proceed any more after removal of the catalyst. Meanwhile ICP-MS analysis on the reaction mixture further verifies no leaching of metals from the catalyst. Furthermore, TEM, XPS and pyridine-adsorbed IR analyses evidence almost unchanged catalytic properties between the fresh and the used Co@Nb-Pt catalysts (Fig. S8). These results can probably explain the superior stability and reusability of this catalyst.

In short, the developed Co@Nb-Pt catalyst shows excellent performance for the base-free aerobic oxidation of HMF to FDCA in water. In the literature, all the benchmark Pt-supported catalysts are active and selective, showing 96–100% yield of FDCA (Table 1). Thereby, in order to compare the catalytic efficiency among different Pt catalysts in a straightforward way, the productivity of FDCA defined as mmol_{FDCA} mol_{Pt}⁻¹ h⁻¹ (P) can be used as a simplified and effective index to

quantitatively describe the activity of each Pt atom for producing FDCA in a unit time. Nonetheless, the influence of reaction temperature as well as O₂ pressure cannot be disregarded. Compared to a Pt/CNT (7.0 P) and a Pt/ZrO₂ catalyst (5.8 P) working at low temperatures of 95 °C and 100 °C, the present Co@Nb-Pt catalyst provides much higher productivity (16.7 P) at 100 °C. This can be owing to the fast response of this catalyst. Compared to other benchmark Pt catalysts all working at 110 °C and 10 bar of O₂, the present catalyst still shows similar but superior productivity (25.0 P), such as a Pt/PVP-ACS (21.8 P) and a Pt/NiO (22.2 P) catalyst.

4. Conclusions

In summary, we report for the first time a Co@Nb bimetallic oxide supported-Pt catalyst for the base-free aerobic oxidation of HMF to FDCA in water. A highest productivity (25 mmol_{FDCA} mol_{Pt}⁻¹ h⁻¹) at > 99% yield of FDCA is attained in the literature to date. We rationally unravel the correlation between the intrinsic activity and selectivity of Co@Nb-Pt catalyst and its unique surface properties. We demonstrate that constructing the Nb⁵⁺-enriched surface on Co-Nb bimetallic oxide can create sufficient Lewis acidic sites and also help stabilize abundant active electron-rich Pt⁰ sites. We further disclose that Pt atoms with high electron density in corporation with electron-deficient Nb⁵⁺ species enable effective adsorption and activation of the C=O and OH bonds through a lower energy barrier, thus accelerating the initial conversion rates of HMF, DFF and FFCA. We believe that our finding may shed light on developing novel and efficient heterogeneous catalysts for selective conversion of biomass.

CRedit authorship contribution statement

Hao Zhang: Conceptualization, Investigation, Methodology, Formal analysis, Writing – original draft preparation. **Runze Zhang:** Investigation, Formal analysis. **Wendi Zhang:** Formal analysis. **Bang Gu:** Supervision. **Qinghu Tang:** Funding acquisition. **Qiue Cao:** Resources, Supervision. **Wenhao Fang:** Conceptualization, Resources, Supervision, Writing – review & editing, Project administration, Funding acquisition.

Declaration of Competing Interest

The authors declare that they have no known competing financial interests or personal relationships that could have appeared to influence the work reported in this paper.

Data availability

Data will be made available on request.

Acknowledgments

This work was supported by the National Natural Science Foundation of China (22272149, 22062025, 21763031), the Yunnan Fundamental Research Projects (202001AW070012, 202101AT070171), the Yunnan University's Research Innovation Fund for Graduate Students (KC-22221892), the Open Research Fund of School of Chemistry and Chemical Engineering of Henan Normal University, the Workstation of Academician Chen Jing of Yunnan Province (202105AF150012), and the Free Exploration Fund for Academician (202305AA160007). The authors thank Advanced Analysis and Measurement Center of Yunnan University for the sample testing service.

Appendix A. Supporting information

Supplementary data associated with this article can be found in the online version at [doi:10.1016/j.apcatb.2023.122670](https://doi.org/10.1016/j.apcatb.2023.122670).

References

- [1] S. Chen, R. Wojcieszak, F. Dumeignil, E. Marceau, S. Royer, How catalysts and experimental conditions determine the selective hydroconversion of furfural and 5-hydroxymethylfurfural, *Chem. Rev.* 118 (2018) 11023–11117.
- [2] Y. Feng, S. Long, X. Tang, Y. Sun, R. Luque, X. Zeng, L. Lin, Earth-abundant 3d-transition-metal catalysts for lignocellulosic biomass conversion, *Chem. Soc. Rev.* 50 (2021) 6042–6093.
- [3] X. Wu, N. Luo, S. Xie, H. Zhang, Q. Zhang, F. Wang, Y. Wang, Photocatalytic transformations of lignocellulosic biomass into chemicals, *Chem. Soc. Rev.* 49 (2020) 6198–6223.
- [4] Y. Dou, M. Zhang, S. Zhou, C. Oldani, W. Fang, Q. Cao, Etherification of 5-hydroxymethylfurfural to biofuel additive catalyzed by Aquivion® PFSA modified mesoporous silica, *Eur. J. Inorg. Chem.* 2018 (2018) 3706–3716.
- [5] Y. Wang, Y. Wang, Y. Lu, Q. Cao, W. Fang, Efficient hydrogenation of 5-hydroxymethylfurfural using a synergistically bimetallic Ru–Ir/C catalyst, *Chem. Commun.* 57 (2021) 1742–1745.
- [6] W. Xie, B. Chen, W. Jia, H. Liu, Z. Li, S. Yang, X. Tang, X. Zeng, Y. Sun, X. Ke, T. Li, H. Fang, L. Lin, Base-free oxidative esterification of 5-hydroxymethylfurfural to furan-2,5-dimethylcarboxylate over n-doped carbon-supported Co/Fe bimetallic catalyst under batch-operation or continuous-flow conditions, *J. Energy Chem.* 75 (2022) 95–108.
- [7] Z. Chen, H. Zhou, F. Kong, M. Wang, Piezocatalytic oxidation of 5-hydroxymethylfurfural to 5-formyl-2-furancarboxylic acid over Pt decorated hydroxyapatite, *Appl. Catal. B* 309 (2022), 121281.
- [8] X.-Q. Pan, X.-Y. Zhang, G.-X. Huang, S.-C. Mei, J.-W. Huang, J.-J. Chen, W.-J. Liu, H.-Q. Yu, Promoting electrocatalytic hydrogenation of 5-hydroxymethylfurfural using buffer electrolytes as proton-donating motifs: Theoretical predictions and experimental validations, *Appl. Catal. B* 323 (2023), 122191.
- [9] Y. Song, Z. Li, K. Fan, Z. Ren, W. Xie, Y. Yang, M. Shao, M. Wei, Ultrathin layered double hydroxides nanosheets array towards efficient electrooxidation of 5-hydroxymethylfurfural coupled with hydrogen generation, *Appl. Catal. B* 299 (2021), 120669.
- [10] R. Luo, Y. Li, L. Xing, N. Wang, R. Zhong, Z. Qian, C. Du, G. Yin, Y. Wang, L. Du, A dynamic Ni(OH)₂-NiOOH/NiFeP heterojunction enabling high-performance E-upgrading of hydroxymethylfurfural, *Appl. Catal. B* 311 (2022), 121357.
- [11] Y. Song, W. Xie, Y. Song, H. Li, S. Li, S. Jiang, J.Y. Lee, M. Shao, Bifunctional integrated electrode for high-efficient hydrogen production coupled with 5-hydroxymethylfurfural oxidation, *Appl. Catal. B* 312 (2022), 121400.
- [12] Y. Zhou, Y. Shen, H. Li, Mechanistic study on electro-oxidation of 5-hydroxymethylfurfural and water molecules via operando surface-enhanced Raman spectroscopy coupled with an Fe³⁺ probe, *Appl. Catal. B* 317 (2022), 121776.
- [13] H. Zhang, Y. Wang, Q. Zhang, B. Gu, Q. Tang, Q. Cao, K. Wei, W. Fang, Synergy in magnetic Ni₂Co₂O₄ oxides enables base-free selective oxidation of 5-hydroxymethylfurfural on loaded Au nanoparticles, *J. Energy Chem.* 78 (2023) 526–536.
- [14] T. Gao, H. Zhang, C. Hu, F. Jing, W. Fang, Base-Free Aerobic Oxidation of 5-Hydroxymethylfurfural on a Ru(II) Center in Cooperation with a Co(II)/Co(III) Redox Pair over the One-Pot Synthesized Ru–Co Composites, *Ind. Eng. Chem. Res.* 59 (2020) 17200–17209.
- [15] A.F. Sousa, C. Vilela, A.C. Fonseca, M. Matos, C.S.R. Freire, G.-J.M. Gruter, J.F. J. Coelho, A.J.D. Silvestre, Biobased polyesters and other polymers from 2,5-furandicarboxylic acid: a tribute to furan excellency, *Polym. Chem.* 6 (2015) 5961–5983.
- [16] X. Wan, C. Zhou, J. Chen, W. Deng, Q. Zhang, Y. Yang, Y. Wang, Base-Free Aerobic Oxidation of 5-Hydroxymethyl-furfural to 2,5-Furandicarboxylic Acid in Water Catalyzed by Functionalized Carbon Nanotube-Supported Au–Pd Alloy Nanoparticles, *ACS Catal.* 4 (2014) 2175–2185.
- [17] T. Gao, J. Chen, W. Fang, Q. Cao, W. Su, F. Dumeignil, Ru/Mn_xCe_{1-x}O_y catalysts with enhanced oxygen mobility and strong metal-support interaction: Exceptional performances in 5-hydroxymethylfurfural base-free aerobic oxidation, *J. Catal.* 368 (2018) 53–68.
- [18] M. Sajid, X. Zhao, D. Liu, Production of 2,5-furandicarboxylic acid (FDCA) from 5-hydroxymethylfurfural (HMF): recent progress focusing on the chemical-catalytic routes, *Green. Chem.* 20 (2018) 5427–5453.
- [19] C. Chen, L. Wang, B. Zhu, Z. Zhou, S.I. El-Hout, J. Yang, J. Zhang, 2,5-Furandicarboxylic acid production via catalytic oxidation of 5-hydroxymethylfurfural: Catalysts, processes and reaction mechanism, *J. Energy Chem.* 54 (2021) 528–554.
- [20] C. Zhou, W. Deng, X. Wan, Q. Zhang, Y. Yang, Y. Wang, Functionalized Carbon Nanotubes for Biomass Conversion: The Base-Free Aerobic Oxidation of 5-Hydroxymethylfurfural to 2,5-Furandicarboxylic Acid over Platinum Supported on a Carbon Nanotube Catalyst, *ChemCatChem* 7 (2015) 2853–2863.
- [21] X. Han, C. Li, Y. Guo, X. Liu, Y. Zhang, Y. Wang, N-doped carbon supported Pt catalyst for base-free oxidation of 5-hydroxymethylfurfural to 2,5-furandicarboxylic acid, *Appl. Catal. A* 526 (2016) 1–8.
- [22] H. Yu, K.-A. Kim, M.J. Kang, S.Y. Hwang, H.G. Cha, Carbon support with tunable porosity prepared by carbonizing chitosan for catalytic oxidation of 5-hydroxymethylfurfural, *ACS Sustain. Chem. Eng.* 7 (2019) 3742–3748.
- [23] H. Chen, J. Shen, K. Chen, Y. Qin, X. Lu, P. Ouyang, J. Fu, Atomic layer deposition of Pt nanoparticles on low surface area zirconium oxide for the efficient base-free oxidation of 5-hydroxymethylfurfural to 2,5-furandicarboxylic acid, *Appl. Catal. A* 555 (2018) 98–107.
- [24] H. Zhang, T. Gao, Q. Cao, W. Fang, Tailoring the Reactive Oxygen Species in Mesoporous NiO for Selectivity-Controlled Aerobic Oxidation of 5-Hydroxymethylfurfural on a Loaded Pt Catalyst, *ACS Sustain. Chem. Eng.* 9 (2021) 6056–6067.
- [25] X. Han, L. Geng, Y. Guo, R. Jia, X. Liu, Y. Zhang, Y. Wang, Base-free aerobic oxidation of 5-hydroxymethylfurfural to 2,5-furandicarboxylic acid over a Pt/C–O–Mg catalyst, *Green. Chem.* 18 (2016) 1597–1604.
- [26] C. Ke, M. Li, G. Fan, L. Yang, F. Li, Pt Nanoparticles Supported on Nitrogen-Doped Carbon-Decorated CeO₂ for Base-Free Aerobic Oxidation of 5-Hydroxymethylfurfural, *Chem. Asian J.* 13 (2018) 2714–2722.
- [27] Y.M.A. Yamada, T. Arakawa, H. Hocke, Y. Uozumi, A. Nanoplatinum, Catalyst for aerobic oxidation of alcohols in water, *Angew. Chem. Int. Ed.* 46 (2007) 704–706.
- [28] S. Siankevich, G. Savoglidis, Z. Fei, G. Laurenczy, D.T.L. Alexander, N. Yan, P. J. Dyson, A novel platinum nanocatalyst for the oxidation of 5-Hydroxymethylfurfural into 2,5-Furandicarboxylic acid under mild conditions, *J. Catal.* 315 (2014) 67–74.
- [29] D.K. Mishra, H.J. Lee, J. Kim, H.-S. Lee, J.K. Cho, Y.-W. Suh, Y. Yi, Y.J. Kim, MnCo₂O₄ spinel supported ruthenium catalyst for air-oxidation of HMF to FDCA under aqueous phase and base-free conditions, *Green. Chem.* 19 (2017) 1619–1623.
- [30] T. Gao, Y. Yin, G. Zhu, Q. Cao, W. Fang, Co₃O₄ NPs decorated Mn–Co–O solid solution as highly selective catalyst for aerobic base-free oxidation of 5-HMF to 2,5-FDCA in water, *Catal. Today* 355 (2020) 252–262.
- [31] J. Chen, W. Sun, Y. Wang, W. Fang, Performant Au hydrogenation catalyst cooperated with Cu-doped Al₂O₃ for selective conversion of furfural to furfuryl alcohol at ambient pressure, *Green Energy Environ.* 6 (2021) 546–556.
- [32] Y. Lu, Y. Wang, Q. Tang, Q. Cao, W. Fang, Synergy in Sn–Mn oxide boosting the hydrogenation catalysis of supported Pt nanoparticles for selective conversion of levulinic acid, *Appl. Catal. B* 300 (2022), 120746.
- [33] Y. Li, H. Chen, L. Chen, Y. Zhang, Y. Mi, M. Liao, W. Liu, D. Wu, Z. Li, H. Peng, Ternary MnCoVO₄ catalysts with remarkable deNO_x performance: Dual acid-redox sites control strategy, *Appl. Catal. B* 318 (2022), 121779.
- [34] M. Jiang, D. Yan, X. Lv, Y. Gao, H. Jia, Recognition of water-dissociation effect toward lattice oxygen activation on single-atom Co catalyst in toluene oxidation, *Appl. Catal. B* 319 (2022), 121962.
- [35] M. Ozawa, M. Takahashi-Morita, K. Kobayashi, M. Haneda, Core-shell type ceria zirconia support for platinum and rhodium three way catalysts, *Catal. Today* 281 (2017) 482–489.
- [36] W. Guan, X. Chen, C.W. Tsang, H. Hu, C. Liang, Highly Dispersed Rh/NbO_x Invoking High Catalytic Performances for the Valorization of Lignin Monophenols and Lignin Oil into Aromatics, *ACS Sustain. Chem. Eng.* 9 (2021) 3529–3541.
- [37] W. Fan, Q. Zhang, W. Deng, Y. Wang, Niobic acid nanosheets synthesized by a simple hydrothermal method as efficient brønsted acid catalysts, *Chem. Mater.* 25 (2013) 3277–3287.
- [38] Y. Wang, T. Gao, Y. Lu, Y. Wang, Q. Cao, W. Fang, Efficient hydrogenation of furfural to furfuryl alcohol by magnetically recoverable RuCo bimetallic catalyst, *Green Energy Environ.* 7 (2022) 275–287.
- [39] W. Ding, H. Peng, W. Zhong, L. Mao, D. Yin, Site-specific catalytic activities to facilitate solvent-free aerobic oxidation of cyclohexylamine to cyclohexanone oxime over highly efficient Nb-modified SBA-15 catalysts, *Catal. Sci. Technol.* 10 (2020) 3409–3422.
- [40] Y. Zhang, S. Wei, Y. Lin, G. Fan, F. Li, Dispersing metallic platinum on green rust enables effective and selective hydrogenation of carbonyl group in cinnamaldehyde, *ACS Omega* 3 (2018) 12778–12787.

- [41] Z. Su, B. Zhang, X. Cheng, F. Zhang, Q. Wan, L. Liu, X. Tan, D. Tan, L. Zheng, J. Zhang, Ultra-small UiO-66-NH₂ nanoparticles immobilized on g-C₃N₄ nanosheets for enhanced catalytic activity, *Green, Energy Environ.* 7 (2022) 512–518.
- [42] H. Liu, X. Cao, J. Wei, W. Jia, M. Li, X. Tang, X. Zeng, Y. Sun, T. Lei, S. Liu, L. Lin, Efficient Aerobic Oxidation of 5-Hydroxymethylfurfural to 2,5-Diformylfuran over Fe₂O₃-Promoted MnO₂ Catalyst, *ACS Sustain. Chem. Eng.* 7 (2019) 7812–7822.
- [43] A. Tirsoaga, M. El Fergani, N. Nuns, P. Simon, P. Granger, V.I. Parvulescu, S. M. Coman, Multifunctional nanocomposites with non-precious metals and magnetic core for 5-HMF oxidation to FDCA, *Appl. Catal. B* 278 (2020), 119309.
- [44] Q. Wang, J. Feng, L. Zheng, B. Wang, R. Bi, Y. He, H. Liu, D. Li, Interfacial Structure-Determined Reaction Pathway and Selectivity for 5-(Hydroxymethyl) furfural Hydrogenation over Cu-Based Catalysts, *ACS Catal.* 10 (2020) 1353–1365.
- [45] X. Meng, Y. Yang, L. Chen, M. Xu, X. Zhang, M. Wei, A Control over Hydrogenation Selectivity of Furfural via Tuning Exposed Facet of Ni Catalysts, *ACS Catal.* 9 (2019) 4226–4235.
- [46] H. Ishikawa, M. Sheng, A. Nakata, K. Nakajima, S. Yamazoe, J. Yamasaki, S. Yamaguchi, T. Mizugaki, T. Mitsudome, Air-stable and reusable cobalt phosphide nanoalloy catalyst for selective hydrogenation of furfural derivatives, *ACS Catal.* 11 (2021) 750–757.
- [47] J. Ren, K.-h Song, Z. Li, Q. Wang, J. Li, Y. Wang, D. Li, C.K. Kim, Activation of formyl CH and hydroxyl OH bonds in HMF by the CuO(111) and Co₃O₄(110) surfaces: A DFT study, *Appl. Surf. Sci.* 456 (2018) 174–183.
- [48] N.R. Avery, EELS identification of the adsorbed species from acetone adsorption on Pt(111), *Surf. Sci.* 125 (1983) 771–786.
- [49] M.S. Ide, R.J. Davis, Perspectives on the kinetics of diol oxidation over supported platinum catalysts in aqueous solution, *J. Catal.* 308 (2013) 50–59.
- [50] J. Chen, Q. Zhang, W. Fang, Y. Wang, H. Wan, Oxidant-free dehydrogenation of alcohols over hydrotalcite-supported palladium catalysts, *Chin. J. Catal.* 31 (2010) 1061–1070.